PAPER • OPEN ACCESS

In-situ formation and evolution of atomic defects in monolayer WSe$_2$ under electron irradiation

View the article online for updates and enhancements.

In-situ formation and evolution of atomic defects in monolayer WSe$_2$ under electron irradiation

Robert Leiter, Yueliang Li and Ute Kaiser

Electron Microscopy Group of Materials Science, Ulm University, Albert-Einstein-Allee 11, 89081, Ulm, Germany

E-mail: yueliang.li@uni-ulm.de

CrossMark

Abstract

Transition metal dichalcogenide (TMD) monolayers such as MoS$_2$, MoSe$_2$, MoTe$_2$, WS$_2$ and WSe$_2$ have attracted significant interest due to their remarkable electronic and optical properties, exhibiting a direct band gap, enabling usability in electronics and optics. Their properties can be altered further by the introduction of lattice defects. In this work, the dynamics of the formation of electron-beam-induced lattice defects in monolayer WSe$_2$ are investigated by *in-situ* spherical and chromatic aberration-corrected low-voltage transmission electron microscopy. We show and analyze the electron-dose-limited life of a monolayer WSe$_2$ from the formation of isolated Se vacancies over extended defects such as vacancy lines, mirror twin boundaries (MTBs) and inversion domains towards the loss of W atoms leading to the formation of holes and finally the destruction of the monolayer. We identify, moreover, a new type of MTB. Our study extends the basic understanding of defect dynamics in monolayer WSe$_2$, sheds further light on the electron radiation response and suggests new ways for engineering the in-plane architecture of TMDs.

Keywords: TMD monolayer, high-resolution transmission electron microscopy, defect engineering

Supplementary material for this article is available online

(Some figures may appear in colour only in the online journal)

1. Introduction

After the discovery of graphene, two-dimensional transition metal dichalcogenides (2D-TMDs) have received increasing attention. Similar to graphite, layers are weakly bound by van-der-Waals bonds, and TMD monolayers can be exfoliated [1]. Extraordinary mechanical, electrical, magnetic and optical properties are reported for 2D-TMDs [2, 3]. Among numerous members of the class of 2D-TMDs, tungsten diselenide (WSe$_2$) is a very promising candidate with a wide range of optoelectronic applications [4–10]. For instance, it opens its direct bandgap from 1.2 eV in bulk [11] to 1.7 eV in the mono-layer structure [12]. Separate band minima make it moreover potentially interesting for quantum information processing [13]. WSe$_2$ can also work as a saturable absorber for pulsed fiber lasers [14].

The formation of lattice defects can modify the properties of TMD monolayers in addition. For example, point defects are shown to create localized excitons in monolayer WSe$_2$ [15]. These states can not only arise from the growth process of the crystal [16] but can also be created afterwards, for example, by electron irradiation via several mechanisms of transferring energy from the impinging electrons to the lattice [17, 18];

those pathways can in principle be followed atom-by-atom if the resolution of the transmission electron microscope (TEM) is sufficient.

Due to the lower atomic number of Se compared to W, Se atoms are more prone to be ejected from the WSe_2 lattice by electron irradiation, which results in the formation of single Se vacancies as well as double Se vacancy columns [19]. By utilizing an electron beam of variable energy, one can even create particular defects. This can, potentially, also be used to tailor unique properties in 2D-TMD materials [20, 21]. It has already been reported that with increased total electron dose, more and more complex defect structures form [22, 23]. Some of these defects agglomerate to line-shaped structures, so called line defects [24, 25], which affect the electronic structure and in some cases even add magnetic moments [26]. The orientation of the line defects can be controlled by directional strain on the material [24]. Mirror twin boundaries (MTBs) are one type of these line defects which have been intensively studied recently [27–35]. One of the reasons for the interest in MTBs is the change of the material properties they cause. Lin *et al* [20] have recently shown that MTBs give rise to p-type doping and local magnetic moments in WSe_2. Thus far, three different types of MTBs have been observed in TMDs, commonly denoted as 4|4P, 4|4E and 55×8 [33]. In the case of WSe_2, only the 55×8 type has been observed at high temperatures of 500 °C [20].

To image structural changes on the level of the single atoms, the resolution of medium-voltage-ranged TEM and scanning TEM (STEM) has been dramatically improved in recent years due to the realization of spherical aberration (C_S) correction of the imaging lenses [36, 37]. However, at medium electron accelerating voltages of 200–300 kV, electron-beam-sensitive 2D materials are often fast destroyed during imaging due to knock-on collusions between the electrons and the atoms. Decreasing knock-on damage while maintaining atomic resolution has been the driving force behind decreasing the voltage, at which the TEM operates down to 20 kV and corrects not only the C_S but also the chromatic aberration (C_C) of the objective lens [38, 39]. C_S- and C_C-corrected TEM is especially useful to study the dynamics of 2D materials at lower accelerating voltages in high-resolution TEM (HRTEM) mode, as it allows, in contrast to the STEM mode, to track the structural rearrangements atom-by-atom in real time, while maintaining a large field of view in a single exposure and collecting the information from all scattered electrons.

Here, we report the formation and evolution of defects in monolayer WSe_2 at room temperature, including all three types of MTBs as well as a fourth type, which was not observed in TMDs so far. We also report on the evolution of the defects with continued electron irradiation from single Se vacancies over extended defects to the rupture of the monolayer.

2. Method

WSe_2 monolayers were prepared by mechanical exfoliation using a Nitto wafer tape. After applying the flakes to a silicon dioxide wafer, suitable monolayers were identified by their contrast in the optical microscope, which is about 40% on a 90 nm SiO_2 coated Si wafer [40, 41]. Subsequently a Quantifoil 0.6/1 TEM grid was placed on top of the area of interest by means of a micromanipulator and brought into contact by an evaporating drop of isopropyl alcohol. The flake and grid were then removed by etching the substrate with potassium hydroxide. The grids were finally washed in distilled water.

We applied the Sub-Angstrom Low-Voltage Electron microscopy (SALVE) instrument at an electron acceleration voltage of 80 kV [39, 42]. The SALVE microscope is corrected for axial geometric aberrations up to fifth order, off-axial geometric aberrations up to third order and chromatic aberrations in the first order, which enables to achieve a resolution of 0.76 Å at 80 kV at a large field of view in a single image [39]. To maximize the atom contrast, we worked in bright atom contrast condition [43]. Here we used a slightly negative C_S of about -7 μm to optimize contrast transfer function with respect to the measured C_5 of about 2 mm. C_C was corrected to about 10 μm. To record the data, we used the 2 k x 2 k camera of the Gatan image filter system. Throughout this paper, we will not only refer to the total accumulated electron dose, but also time passed between subsequent images for clarity of the figures. For image simulations, we used the QSTEM software package [44]. The dampening of the contrast induced by the camera was included by adding the corresponding modulation transfer function (MTF) to the simulated images. The MTF of the camera was prior measured using single pixel illumination as described by Lubk *et al* [45]. The effect of limited electron dose was emulated by applying noise to the calculated images using a custom script for Gatan DigitalMicrograph based on Monte-Carlo methods and exploiting the Poisson statistics of electrons.

3. Results and discussion

We start our discussion with presenting the monolayer flake of WSe_2 used for TEM investigation, which is denoted by the white arrow in figure 1(a), and the structural model in plan- and side view shown in figure 1(c). Here we introduce single Se vacancy and double Se vacancy column and their schematic used later in the manuscript. Figure 1(b) shows the initial 80 kV C_C/C_S-corrected HRTEM image of the monolayer WSe_2. The Se_2 atom columns with 2 Se atoms produce higher contrast than one W atom (W mass is 183.84 u, Se mass is 78.97 u, for explanation see supplementary figure S2) [46].

After accumulating a higher electron dose of 1.0×10^8 e$^-$/nm^2 on the specimen, which is about a factor of 1000 higher compared to the initial image presented in figure 1(b), we observe the formation of single Se vacancies which tend to transfer into double Se vacancy columns (figure 2(a)). Here we inserted in the right upper corner a simulated image with one double Se vacancy column and one single Se vacancy, using the experimental parameters as described in the method section. One can identify the positions of W and Se and distinguish double Se vacancy columns from single Se vacancies (see the agreement between the red (calculation) and green (experiment) line profiles through single Se vacancy and double Se vacancy column). By comparing subsequent images
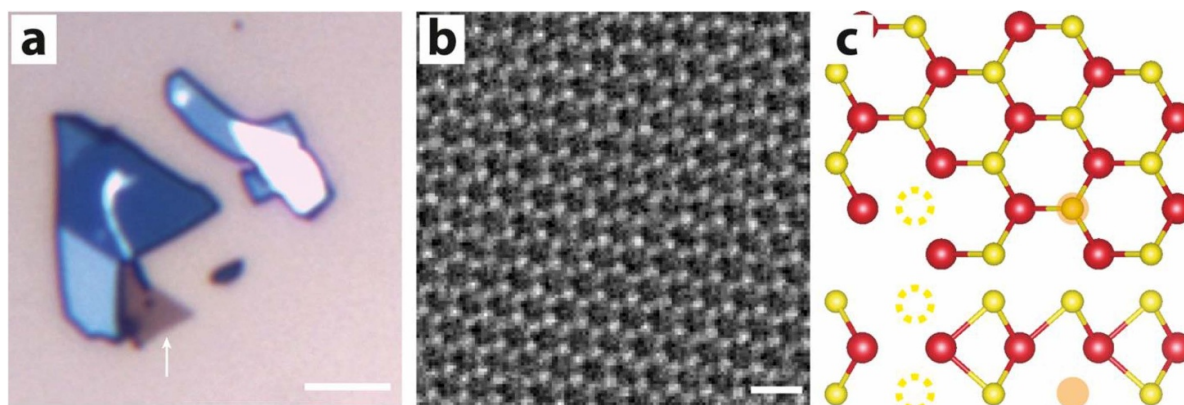
Figure 1. (a) Optical micrograph of few-layer WSe$_2$ on a SiO$_2$ substrate. The monolayer WSe$_2$ is marked with a white arrow. Scale bar is 5 μm. (b) 80 kV C_C/C_S-corrected HRTEM image showing the initial state of the monolayer WSe$_2$, showing a predominantly intact layer. The brighter atom contrast originates from the two Se atoms underneath each other (compare the model in (c) and see supplementary figure S2 (available online at stacks.iop.org/NANO/31/495704/mmedia) for explanation). The electron dose is 2.9 × 10^5 e$^-$/nm^2, scale bar is 5 Å. (c) shows the atomic model of a monolayer WSe$_2$, which is structurally identical in most TMDs: The W atoms (marked red) sit in the center of the film, while the Se atoms (marked yellow) stacked on top of each other. Together they form a hexagonal structure when observed from above. Single and double Se vacancies are marked by orange circle and yellow dotted circle, respectively, which will be further discussed in the text.
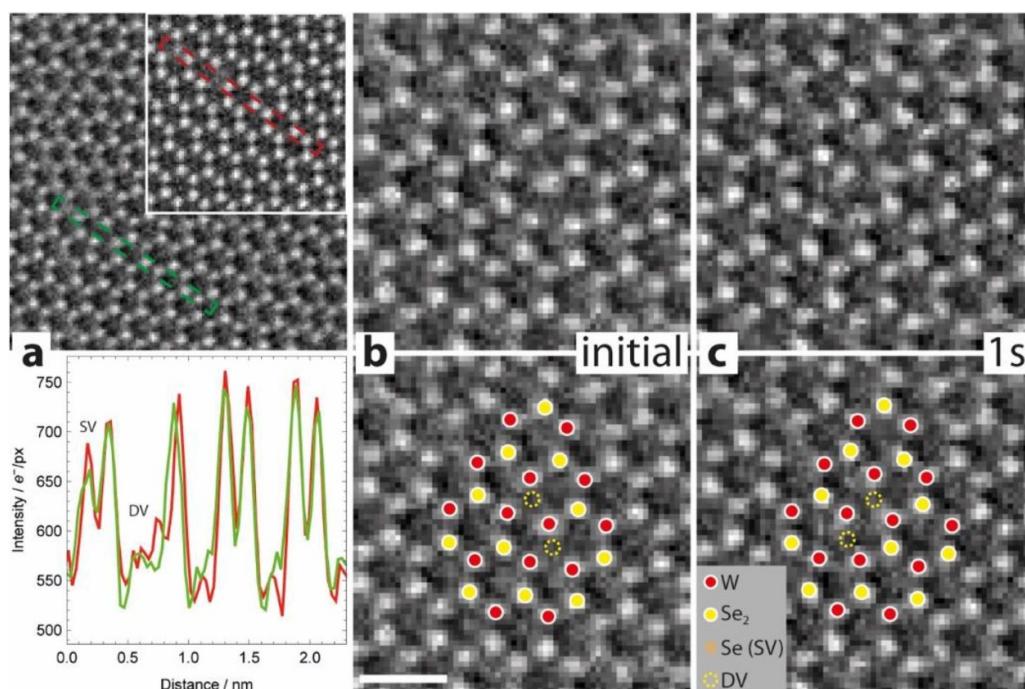

Figure 2. Early stages of electron irradiation damage. (a) 80 kV C_C/C_S-corrected HRTEM image of an area with single and double Se vacancies (top) with corresponding HRTEM image simulation (inset) and intensity profiles showing good agreement between experiment and simulation. The green profile was taken from the correspondingly marked area in the experimental image, while the red profile is from the simulation. Dose rate is 6.2 × 10^5 e$^-$/nm^{2}s in this and all subsequent images. Note that due to the low electron dose, the height of the peaks varies due to the random nature of the noise. In addition, the relatively low sampling rate affects the shape of the peaks. In general, the Se$_2$ columns appear brighter than a W atom despite their added mass being lower (for details, see supplementary information). (b) and (c), as well as the following figures, show the unfiltered raw images in the top row and the same images with an overlay of the proposed atomic structure in the lower row. (b) Initial state showing two different double vacancies of Se in close proximity. (c) The next frame, 1 s later, shows the double vacancy filled up by neighboring atoms, therefore leaving another double vacancy in a nearby position, showing the high mobility of Se atoms. See supplementary movie 2 for the whole evolution. Scale bar is 5 Å.

of our image series, we observe a high mobility of double Se vacancy columns, resulting in back and forth jumping of double Se vacancy columns as exemplified in figures 2(b), (c) and figure S1 (supplementary information), as well as supplementary movie 2. This can be explained by the low energy barrier for migration in WSe$_2$, as was already reported in literature [27, 47].

As Se atoms continue to be ejected under further electron irradiation, more complex extended defect structures evolve. Figure 3 shows the formation of a symmetric trefoil defect,
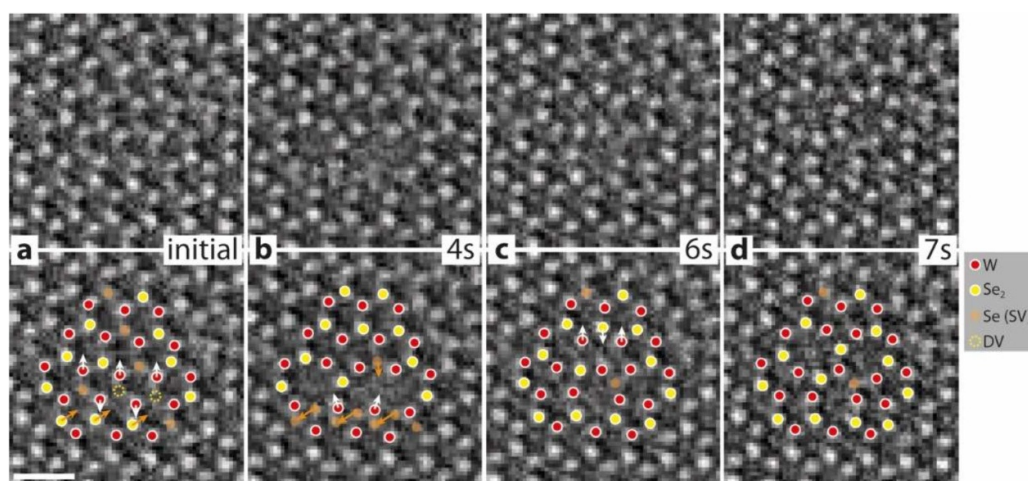
Figure 3. 80 kV C_C/C_S-corrected HRTEM images showing the formation of a trefoil defect in monolayer WSe_2. For better understanding of the defect formation, the lower raw depicts the same images as above with marked atoms (see the legend). (a) Initial state showing several single and double vacancies in close proximity, as marked by transparent orange dots and a broken yellow circle, respectively. (b) After 4 s, rearrangement starts in the lower part of the image, where the W atoms move outward while one Se_2 column moves inward, thus creating two irregularly shaped rings. Additionally, a staggered double vacancy line is formed by rearrangement of the Se atoms in the lower part of the image. (c) After 6 s, the first ring of the final structure is formed. This is due to the recombination of the staggered atoms in the vacancy line, leaving three isolated double vacancies as well as an upwards move of the second row of W atoms from the bottom. (d) After 7 s, the trefoil structure moves to its final state by a downwards move of the Se_2 column in the top center and a simultaneous upwards move of the neighboring two W atoms. Dose rate is 6.2×10^5 e$^-$/nm^{2}s. See supplementary movie 3 for the whole evolution. Scale bar is 5 Å.
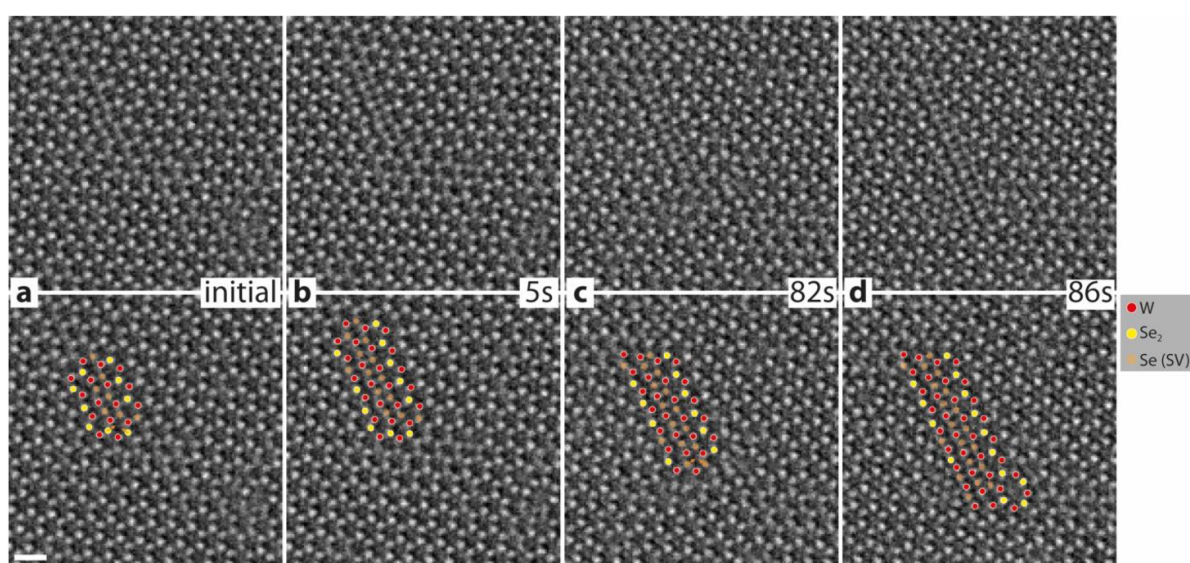

Figure 4. 80 kV C_C/C_S-corrected HRTEM images showing the growth of a staggered double vacancy line in monolayer WSe_2. For better understanding of the defect formation, the lower raw depicted the same image as above with marked atoms (see the legend). (a) Initial state with the vacancy line consisting of five single Se vacancies. (b) The line defect extends to the top left via the collapse of a hexagon containing single Se vacancies. The number of Se vacancies in the line increases to nine. (c) After being stable for 83 s (5.1×10^7 e$^-$/nm^2), the structure begins to expand to the lower right. In this transitional state, the line defect is terminated by a hexagon containing single Se vacancies and contains a total of 13 Se vacancies including the hexagon. (d) Two more hexagons collapse and form the final state of the line defect with 15 single Se vacancies. Dose rate is 6.2×10^5 e$^-$/nm^{2}s. See supplementary movie 4 for the whole evolution. Scale bar is 5 Å.

which requires a deficit of six Se atoms; in the lower raw of the images the same images are displayed together with the marked atoms for better understanding of the defect formation process. We identify the formation path as a multi-step process, which also includes asymmetric rings as follows: In figure 3(a) two double vacancies form, as well as five single vacancies as shown schematically in the lower image. The

atoms then rearrange (see figure 3(b)) to fill up the voids in the upper part of the structure, while creating two irregularly shaped rings and a staggered double vacancy line again schematically shown in the lower image of figure 3(b). In the next step, the atoms rearrange into one 8-membered ring as marked in the lower image (figure 3(c)). Finally, two more rings are formed by a simple move of one Se_2 column
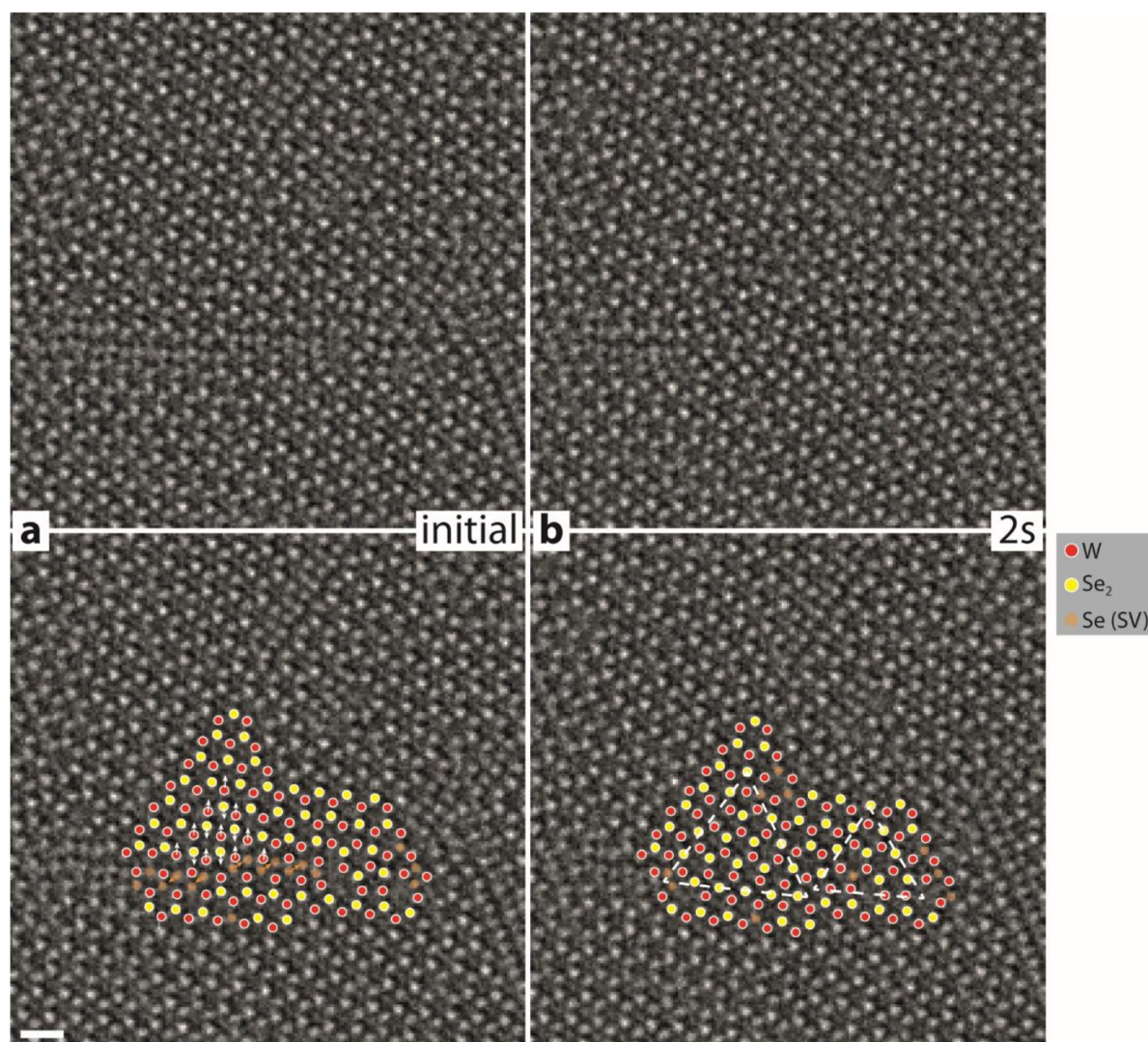
Figure 5. 80 kV C_C/C_S-corrected HRTEM images showing the formation of inversion domains in monolayer WSe_2. For better understanding of the defect formation, the lower raw depicted the same image as above with marked atoms (see the legend). (a) The initial state with two staggered double vacancy lines as marked with orange dots denoting single Se atoms. (b) The Se atoms from the vacancy lines glide into each other and form a 4|4P MTB, while in the central area there is also a glide of both Se planes in one direction and the W plane in the opposite direction, constituting the inversion domain. In this case, all three edges are 4|4P MTBs. Note that one complete double vacancy column is missing from the left MTB. Dose rate is 6.2×10^5 e⁻/nm²s. See supplementary movie 5 for the whole evolution. Scale bar is 5 Å.

down and two W atoms up. This is in contrast to previously suggested formation pathways, requiring a specific triangular arrangement of double vacancies and a subsequent bond rotation [20]. This discrepancy may be associated to the local distribution of missing atoms and therefore may not follow the energetically lowest pathway.

As more and more Se atoms are removed from the lattice we observe line defects consisting of multiple Se vacancies. Figure 4 shows the formation of a 2.3 nm long double Se vacancy line with 15 lost Se atoms. The growth process is driven now by the collapse of hexagons, which contain three single Se vacancies shown in figure 4(a). In this step, the remaining single Se atoms move inward of the former hexagon. This process continues as more vacancies are created by the electron beam. It is conceivable that this process

and the direction of the line growth depends on lattice strain, which is induced by the rigidity of the holey carbon grid supporting the monolayer. Such preferential orientation was previously reported for MoS_2 by Komsa *et al* [24]. Curiously, the growth of the defect pauses for over 1 min or 5.1×10^7 e⁻/nm² in between figures 4(b) and (c), before another interval of rapid growth sets in figures 4(c) and (d).

In the timeframe after the formation of one-dimensional defects (line defects), we begin to observe extended two-dimensional defects. One type of these structures forms as inversion domains, which are terminated with MTBs. An example of such a formation process is shown in figure 5. We observe that in this case, two staggered double vacancy lines glide into each other and recombine by moving the lower Se atoms on top of the ones to the upper right of their respective
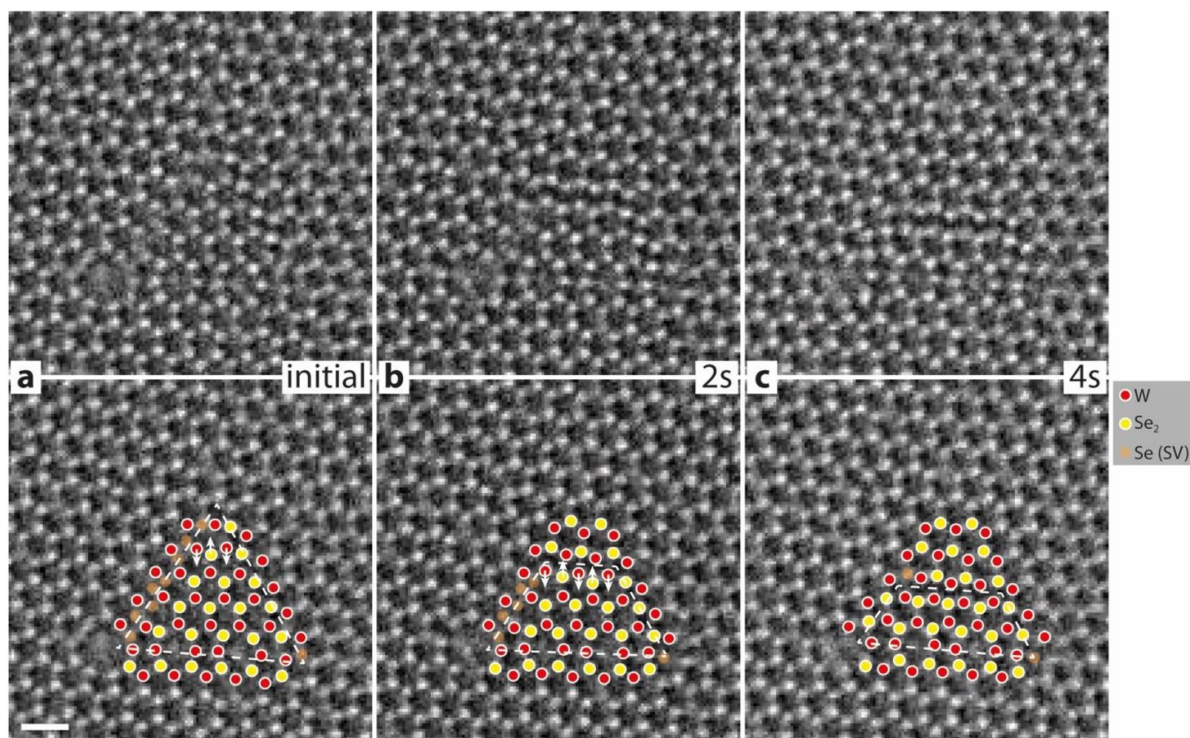
Figure 6. 80 kV C_C/C_S-corrected HRTEM images showing the evolution of an inversion domain with different MTBs in monolayer WSe$_2$. (a) shows 4|4E boundary on the left, 4|4P on the right and 55 × 8 at the bottom. (b) The area of the inversion domain shrinks from the top, which is now delimited by a new type of boundary, which we denote 4|4E′. (c) The area continues to shrink by another row of atoms, thereby extending the new boundary. Dose rate is 6.2×10^5 e$^-$/nm^{2}s. See supplementary movie 6 for the whole evolution. Scale bar is 5 Å.
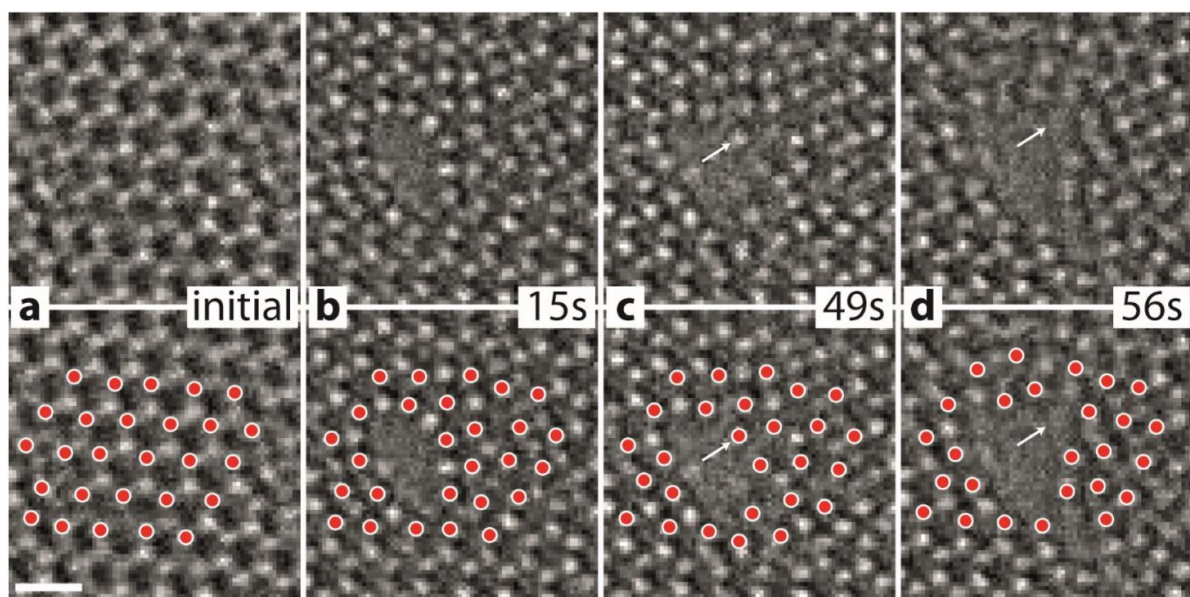

Figure 7. 80 kV C_C/C_S-corrected HRTEM images showing the stability of the W frame under electron irradiation. The number of W atoms in the cluster remains constant in the beginning, while Se atoms are constantly removed from the lattice. This leads to the formation of holes due to the lattice strain. Only with continued irradiation, the first W atom is sputtered after 49 s. W atoms are highlighted in red. Dose rate is 6.2×10^5 e$^-$/nm^{2}s. See supplementary movie 7 for the whole evolution. Scale bar is 5 Å.

positions while the W atoms move down and to the left. This in turn causes a glide of the Se planes against the W plane, were the Se$_2$ columns move down and the W atoms move up within the triangular area seen in figure 5. In this case, the MTBs, which terminate the inversion domain on the left in figure 5(a) are all 4|4P structures. Such a termination has been previously reported for MoS$_2$ and MoSe$_2$, but not in WSe$_2$ [27, 28, 32].

With increased accumulated electron dose, we observe further structural changes for inversion domains and MTBs. In figure 6(a) we observe an inversion domain with all three types of MTBs known in TMDs so far, including not only the 4|4P type on the right, as mentioned above, 55 × 8 at the bottom, but in addition the 4|4E MTB, which also was not found in previous reports on WSe$_2$. 2 s later, we observe the inversion domain to shrink from the top, simultaneously the Se atoms move up and the W atoms move down, resulting in two W planes without Se atoms between. This is a new type of MTB, which appears at the top of the trapezium domain. This MTB has a similar edge type symmetry to the 4|4E structure, but without the staggered single Se atoms in the center. We therefore denote this new type of MTB as 4|4E′. In addition to the shrinkage of the inversion domain and further gliding of the new type of MTB, we observe a change in the left side of the inversion domain, where the MTB changes from 4|4E to 4|4P. We suggest that this evolution of the inversion domain is caused by changes to the strain state of the surrounding lattice. We speculate, that this could lead to the original domain structure being energetically favorable again, similar to the report of Komsa *et al* [24].

As we continued to irradiate the sample, the increasingly strained lattice leads to the formation of holes in the film. Despite this, the W atoms are not sputtered until the local ratio between W and Se approaches 1:1 (figure 7). In figure 7(a), we see the initial state with an already slightly defective, but still continuous layer. As more Se atoms are ejected, a hole starts to form (figure 7(b)). However, the number of W atoms, marked in red, remains the same. This also holds for panel (c), where the size of the hole is extended further as more Se atoms are removed. The W atom marked by the white arrow is the first one, which is removed in figure 7(d). As this occurs, the number of Se atoms has been reduced to about the same as the W atoms. Recently, Zhao *et al* demonstrated the formation of a pure Mo islands within MoS$_2$ [48]. However, their STEM irradiated only a small area on the sample at the same time, keeping the unirradiated area still stoichiometric without defects. In our case, a much larger area was under irradiation. The area was full of defects with loss of many Se atoms at this stage. The strained, almost destroyed monolayer is not compatible with an active pure W cluster. This could explain why we did not observe analogous behavior in our experiments.

4. Conclusion

In conclusion, we have shown atom-by-atom electron-beam-induced and electron-dose-dependent formation and evolution of different defect types in monolayer WSe$_2$. In particular, we have reported the dose-dependent evolution of point defects over line defects, more extended defects to 2D defect structures taking also unusual pathways, which are more complex than suggested from theoretical calculations. Moreover, inversion domains with previously unreported MTBs were formed and it was shown how they developed dynamically with increasing electron dose. As reported earlier, those boundaries are of particular interest with respect to modification of the

electronic properties of the material. With further increased electron dose, highly defective W-rich regions within the WSe$_2$ matrix formed, paving ways towards future device engineering. In general, our study may help to tailor devices composed of defined defect controlled WSe$_2$ monolayers with specific electronic and magnetic properties in the future.

ORCID iD

Yueliang Li https://orcid.org/0000-0002-3583-7586

References

[1] Frindt R F *et al* 1966 Single crystals of MoS$_2$ several molecular layers thick *J. Phys. D: Appl. Phys.* **37** 1928–9
[2] Wang Q H, Kalantar-Zadeh K, Kis A, Coleman J N and Strano M S 2012 Electronics and optoelectronics of two-dimensional transition metal dichalcogenides *Nat. Nanotechnol.* **7** 699–712
[3] Chhowalla M, Shin H S, Eda G, Li L-J, Loh K P and Zhang H 2013 The chemistry of two-dimensional layered transition metal dichalcogenide nanosheets *Nat. Chem.* **5** 263–75
[4] Radisavljevic B, Radenovic A, Brivio J, Giacometti V and Kis A 2011 Single-layer MoS$_2$ transistors *Nat. Nanotechnol.* **6** 147–50
[5] Liu D *et al* 2019 Conformal hexagonal-boron nitride dielectric interface for tungsten diselenide devices with improved mobility and thermal dissipation *Nat. Commun.* **10** 1188
[6] Wang Z *et al* 2018 Selectively plasmon-enhanced second-harmonic generation from monolayer tungsten diselenide on flexible substrates *ACS Nano* **12** 1859–67
[7] Cheng Q *et al* 2020 WSe$_2$ 2D p-type semiconductor-based electronic devices for information technology: design, preparation, and applications *InfoMat* **2** 656–97
[8] De Luca M, Cartoixà X, Martín-Sánchez J, López-Suárez M, Trotta R, Rurali R and Zardo I 2020 New insights in the lattice dynamics of monolayers, bilayers, and trilayers of WSe$_2$ and unambiguous determination of few-layer-flakes' thickness *2D Mater.* **7** 025004
[9] Smyth C M *et al* 2019 Engineering the interface chemistry for scandium electron contacts in WSe$_2$ transistors and diodes *2D Mater.* **6** 045020
[10] Król M *et al* 2019 Exciton-polaritons in multilayer WSe$_2$ in a planar microcavity *2D Mater.* **7** 015006
[11] Kam K K and Parkinson B A 1982 Detailed photocurrent spectroscopy of the semiconducting group VIB transition metal dichalcogenides *J. Phys. Chem.* **86** 463–7
[12] Ding Y, Wang Y, Ni J, Shi L, Shi S and Tang W 2011 First principles study of structural, vibrational and electronic properties of graphene-like MX2 (M=Mo, Nb, W, Ta; X=S, Se, Te) monolayers *Phys. B Condens. Matter* **406** 2254–60
[13] Langer F *et al* 2018 Lightwave valleytronics in a monolayer of tungsten diselenide *Nature* **557** 76–80

[14] Liu W, Liu M, Yin J, Chen H, Lu W, Fang S, Teng H, Lei M, Yan P and Wei Z 2018 Tungsten diselenide for all-fiber lasers with the chemical vapor deposition method *Nanoscale* **10** 7971–7

[15] Zhang S, Wang C-G, Li M-Y, Huang D, Li L-J, Ji W and Wu S 2017 Defect structure of localized excitons in a WSe₂ monolayer *Phys. Rev. Lett.* **119** 046101

[16] Mortelmans W, Nalin Mehta A, Balaji Y, El Kazzi S, Sergeant S, Houssa M, De Gendt S, Heyns M and Merckling C 2020 Fundamental limitation of van der Waals homoepitaxy by stacking fault formation in WSe₂ *2D Mater.* **7** 025027

[17] Algara-Siller G, Kurasch S, Sedighi M, Lehtinen O and Kaiser U 2013 The pristine atomic structure of MoS₂ monolayer protected from electron radiation damage by graphene *Appl. Phys. Lett.* **103** 203107

[18] Lehnert T, Lehtinen O, Algara–Siller G and Kaiser U 2017 Electron radiation damage mechanisms in 2D MoSe₂ *Appl. Phys. Lett.* **110** 033106

[19] Komsa H-P, Kotakoski J, Kurasch S, Lehtinen O, Kaiser U and Krasheninnikov A V 2012 Two-dimensional transition metal dichalcogenides under electron irradiation: defect production and doping *Phys. Rev. Lett.* **109** 035503

[20] Lin Y-C *et al* 2015 Three-fold rotational defects in two-dimensional transition metal dichalcogenides *Nat. Commun.* **6** 6736

[21] Komsa H-P and Krasheninnikov A V 2017 Engineering the electronic properties of two-dimensional transition metal dichalcogenides by introducing mirror twin boundaries *Adv. Electron. Mater.* **3** 1600468

[22] Ryu G H, France-Lanord A, Wen Y, Zhou S, Grossman J C and Warner J H 2018 Atomic structure and dynamics of self-limiting sub-nanometer pores in monolayer WS₂ *ACS Nano* **12** 11638–47

[23] Lu X *et al* 2014 Large-area synthesis of monolayer and few-layer MoSe₂ films on SiO₂ substrates *Nano Lett.* **14** 2419–25

[24] Komsa H-P, Kurasch S, Lehtinen O, Kaiser U and Krasheninnikov A V 2013 From point to extended defects in two-dimensional MoS₂: evolution of atomic structure under electron irradiation *Phys. Rev. B* **88** 035301

[25] Chen Q, Li H, Zhou S, Xu W, Chen J, Sawada H, Allen C S, Kirkland A I, Grossman J C and Warner J H 2018 Ultralong 1D vacancy channels for rapid atomic migration during 2d void formation in monolayer MoS₂ *ACS Nano* **12** 7721–30

[26] Lehnert T, Ghorbani-Asl M, Köster J, Lee Z, Krasheninnikov A V and Kaiser U 2019 Electron-beam-driven structure evolution of single-layer MoTe₂ for quantum devices *ACS Appl. Nano Mater.* **2** 3262–70

[27] Lin J, Pantelides S T and Zhou W 2015 Vacancy-induced formation and growth of inversion domains in transition-metal dichalcogenide monolayer *ACS Nano* **9** 5189–97

[28] Lehtinen O *et al* 2015 Atomic scale microstructure and properties of se-deficient two-dimensional MoSe₂ *ACS Nano* **9** 3274–83

[29] Diaz H C, Ma Y, Chaghi R and Batzill M 2016 High density of (pseudo) periodic twin-grain boundaries in molecular beam epitaxy-grown van der Waals heterostructure: moTe₂ /MoS₂ *Appl. Phys. Lett.* **108** 191606

[30] Liu H *et al* 2014 Dense network of one-dimensional midgap metallic modes in monolayer MoSe₂ and their spatial undulations *Phys. Rev. Lett.* **113** 066105

[31] Barja S *et al* 2016 Charge density wave order in 1D mirror twin boundaries of single-layer MoSe₂ *Nat. Phys.* **12** 751–6

[32] Wang S, Lee G-D, Lee S, Yoon E and Warner J H 2016 Detailed atomic reconstruction of extended line defects in monolayer MoS₂ *ACS Nano* **10** 5419–30

[33] Zhou W, Zou X, Najmaei S, Liu Z, Shi Y, Kong J, Lou J, Ajayan P M, Yakobson B I and Idrobo J-C 2013 Intrinsic structural defects in monolayer molybdenum disulfide *Nano Lett.* **13** 2615–22

[34] T H L, Perello D J, Zhao J, Deng Q, Kim H, Han G H, Chae S H, Jeong H Y and Lee Y H 2016 Misorientation-angle-dependent electrical transport across molybdenum disulfide grain boundaries *Nat. Commun.* **7** 10426

[35] van der Zande A M, Huang P Y, Chenet D A, Berkelbach T C, You Y, Lee G-H, Heinz T F, Reichman D R, Muller D A and Hone J C 2013 Grains and grain boundaries in highly crystalline monolayer molybdenum disulphide *Nat. Mater.* **12** 554–61

[36] Rose H 1990 Outline of a spherically corrected semi-aplanatic medium-voltage transmission electron microscope *Optik* **85** 19–24

[37] Haider M, Uhlemann S, Schwan E, Rose G, Kabius B and Urban K 1998 Electron microscopy image enhanced *Nature* **392** 768–9

[38] Kaiser U *et al* 2011 Transmission electron microscopy at 20kV for imaging and spectroscopy *Ultramicroscopy* **111** 1239–46

[39] Linck M *et al* 2016 Chromatic aberration correction for atomic resolution TEM imaging from 20 to 80 kV *Phys. Rev. Lett.* **117** 076101

[40] Blake P, Hill E W, Castro Neto A H, Novoselov K S, Jiang D, Yang R, Booth T J and Geim A K 2007 Making graphene visible *Appl. Phys. Lett.* **91** 13–15

[41] Benameur M M, Radisavljevic B, Héron J S, Sahoo S, Berger H and Kis A 2011 Visibility of dichalcogenide nanolayers *Nanotechnology* **22** 125706

[42] The Sub-Angstrom Low-Voltage Electron Microscopy Project www.salve-project.de

[43] Lentzen M 2008 Contrast transfer and resolution limits for sub-angstrom high-resolution transmission electron microscopy *Microsc. Microanal.* **14** 16–26

[44] Koch C 2002 *Determination of the Core Structure Periodicity and Point Defect Density along Dislocations* (Ann Arbor, MI: ProQuest Dissertations Publishing)

[45] Lubk A, Röder F, Niermann T, Gatel C, Joulie S, Houdellier F, Magén C and Hÿtch M J 2012 A new linear transfer theory and characterization method for image detectors. Part II: experiment *Ultramicroscopy* **115** 78–87

[46] Meija J *et al* 2016 Atomic weights of the elements 2013 (IUPAC Technical Report) *Pure Appl. Chem.* **88** 265–91

[47] Lin J *et al* 2014 Flexible metallic nanowires with self-adaptive contacts to semiconducting transition-metal dichalcogenide monolayers *Nat. Nanotechnol.* **9** 436–42

[48] Zhao X, Dan J, Chen J, Ding Z, Zhou W, Loh K P and Pennycook S J 2018 Atom-by-atom fabrication of monolayer molybdenum membranes *Adv. Mater.* **30** 1707281